PERGAMON

International Journal of Heat and Mass Transfer 45 (2002) 3459–3470

International Journal of HEAT and MASS TRANSFER

www.elsevier.com/locate/ijhmt

Thermal convection in a porous toroidal thermosyphon

Y.Y. Jiang *, M. Shoji [1]

Department of Mechanical Engineering, Faculty of Engineering, The University of Tokyo, 7-3-1 Hongo, Bunkyo-ku, Tokyo 113-8656, Japan

Received 11 May 2001

Abstract

Stability of natural convection in porous media differs from that in Newtonian fluid due to the changes of the thermal inertia and the friction. This paper aims to investigate the natural convection and its stability in a toroidal thermosyphon filled with porous media. The flow and temperature fields were numerically simulated and compared with that of Newtonian fluid. The results predicted two obvious local reversal flows near the connections of heating and cooling halves. A one-dimensional model was proposed which described qualitatively the occurring and stability of the thermal convection. The model suggested that the flow stability depends largely on the Prandtl number. The global flow can probably be chaotic only if the Prandtl number is finite. Contradictions of the conclusions drawn by different researchers were also discussed.

Keywords: Thermal convection; Porous media; Thermosyphon; Stability; Numerical research

1. Introduction

Natural (thermal) convection in porous media received broad researches, because of the extensive engineering backgrounds. As a common feature of Bénard–Darcy convection (BDC), the porous layer is subjected to a temperature gradient inverse to the gravity or centrifugal force. Due to the changes of the hydraulic and thermal properties, the stability of porous natural flow differs very much from that of Newtonian flow. The inhomogeneities of the permeability and the thermal conductivity brought about by the presence of the solid substance affects greatly the stability as well.

The time-dependent convective patterns in horizontal porous layers have been studied, on the basis of Darcy's law and related to the instability of the thermal boundary layers [1–10]. This kind of instability dominates in the limit of infinite Prandtl number, that $Pr' \to \infty$. This means that such instability is not affected by the inertia force. If the condition of $1/Pr' = 0$ is relaxed, the stability problem of a different nature is encountered. The thermal inertia force under this condition can act to maintain the flow direction even opposing the buoyant force and bring about the instability of the flow directions, from which chaos arises [11,12]. The chaos prevails in the whole system at large Rayleigh numbers and leads finally to the turbulent flow.

On considering the criteria of the occurring and stability of global convection, some dynamical scenarios were proposed. Those models were derived by one-dimensional Fourier expansion [13] or by two-dimensional Galerkin expansion [11,12] of the governing equations. Sen and Torrance [13] suggested that the global flow is always stable in their annulus. Vadasz and Olek [11] established a two-dimensional model for flow in rotating cavity by the method of Lorenz [14], which numerically predicted a global Lorenz-like unstable flow behavior. The point is, whether the global unstable flow exists in porous media. Early in 1984, Curry et al. [15] showed that the second-order nontrivial truncation of the Galerkin expansion is certainly not valid as a representation of convection. The same problem exists in modeling porous flow. Masuoka [12] simulated the flow behaviors of a two-dimensional porous layer. The results indicated that at small Prandtl numbers, the chaotic

* Corresponding author. Tel.: +81-3-5841-6408; fax: +81-3-5841-6408.

E-mail addresses: yyjiang@photon.t.u-tokyo.ac.jp (Y.Y. Jiang), shoji@photon.t.u-tokyo.ac.jp (M. Shoji).

[1] Tel.: +81-3-5841-6406; fax: +81-3-5841-6406.

0017-9310/02/$ - see front matter
PII: S0017-9310(02)00062-5

Nomenclature

a_e	thermal diffusivity of porous media (m^2/s)
C_E	Ergun constant
C'_E	See Eq. (9)
Da	Darcy number, K/r_0^2
g	gravity accelerator (m/s^2)
h	heat transfer coefficient ($W/(m^2\ °C)$)
h_r, h_φ, h_θ	Lamé coefficients
k	thermal conductivity ($W/(m\ °C)$)
K	permeability (m^2)
Nu	Nusselt number, $(2hr_0)/k_e$
$\overline{\mathbf{Nu}}$	peripherally averaged Nusselt number, $(2\int_0^\pi(\partial\Phi/\partial r)\mid_1 \mathrm{d}\varphi)/\int_0^\pi(\Phi_b-\Phi_w)\mathrm{d}\varphi$
P, P^*	pressure, $P = P^*/(a_e\mu/K)$
Pr	Prandtl number, $\frac{\upsilon_f}{a_e}$
Pr'	equivalent Prandtl number of porous media, $\frac{\sigma\varepsilon}{Da}Pr$.
r^*, r	radial coordinate, $r = r^*/r_0$
r_0	torus section radius (m)
R, R^*	pipe radius of curvature, $R = R^*/r_0$
Ra	Rayleigh number, $(\rho_f g\beta(T_h - T_c)r_0K)/a_e\mu_f$
Re	Reynolds number, $= (2\overline{w^*}r_0)/\upsilon_f = 2\overline{w}/Pr$
$S_{d,u}$, $S_{d,v}$, $S_{d,w}$	see Eqs. (2)–(4)
t, τ	time, $\tau = t/(\sigma r_0^2/a_e)$
T	temperature (°C)
u, u^*	radial velocity, $u = u^*/(a_e/r_0)$
v, v^*	circumferential velocity, $v = v^*/(a_e/r_0)$
w, w^*	axial velocity, $w = w^*/(a_e/r_0)$
$\bar{w}$	cross-sectionally averaged axial velocity, $(1/\pi)\int_0^{2\pi}\int_0^1 wr\mathrm{d}r\mathrm{d}\varphi$
x, y, z	see Eqs. (14)–(16)

Greek symbols

α	tilt angle in vertical plane of the torus
β	thermal expansion coefficient (K^{-1})
ε	porosity of porous media
Φ	dimensionless temperature, $= (T - T_c)/(T_h - T_c)$
Φ_b	bulk temperature, $(1/\bar{w}\pi)\int_0^{2\pi}\int_0^1 w\Phi r\mathrm{d}r\mathrm{d}\varphi$
$\bar{\Phi}$	cross-sectionally averaged temperature, $(1/\pi)\int_0^{2\pi}\int_0^1 \Phi r\mathrm{d}r\mathrm{d}\varphi$
φ, θ	see Fig. 2
λ	eigenvalue of coefficient matrix
μ	dynamic viscosity of fluid (kg/(m s))
ν	kinematical viscosity of fluid (m^2/s)
ρ	density of the fluid (kg/m^3)
σ	capacity ratio of porous media, $((\rho c)_f\varepsilon + (\rho c)_s(1-\varepsilon))/((\rho c)_f)$

Superscript

$*$	variable with dimension

Subscripts

b	bulk
c	cooling, critical value
e	equivalent parameter of porous media
f	fluid
h	heating
r	radial direction
s	solid
φ	circumferential direction
θ	axial direction

flow is thermal inertia dependent where the Lorenz-like chaos is possible. And at large Prandtl numbers, the flow structure is localized. The chaos occurs via intermittency of local flow modes in the thermal boundary layers and is hence different in nature from the former.

On the other hand, the Lorenz-like chaotic alternations of flow direction in Newtonian liquid were experimentally observed in a toroidal thermosyphon [16–18], which was well described by the Lorenz model [17,19]. The phenomenon is undesirable in solar water systems, nuclear reactors and geothermal energy systems etc. Previous researchers tried to eliminate the phenomena either by active control [19,20] or by varying the boundary conditions [21]. Filling the loop with porous media may be another choice, which needs comprehensive examination (the subject of this paper). This work aims to investigate the natural convection in the loop (see Fig. 1) filled with homogeneous porous media. The real flow patterns, the non-Darcian effects on flow behaviors, and the validity of one-dimensional simplifying were discussed according to the numerical results. A one-dimensional model was tentatively proposed,

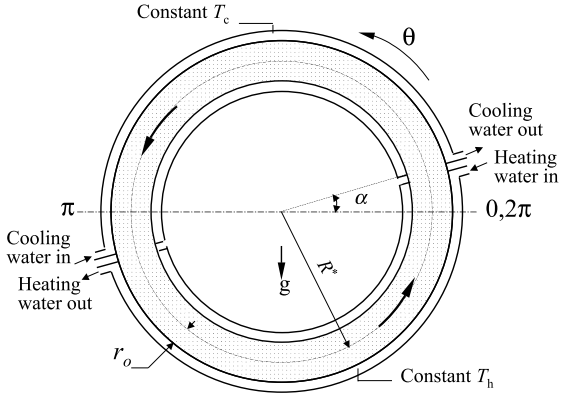

Fig. 1. The toroidal thermosyphon.

which showed that the stability of the global flow in porous media depends largely on the Prandtl number as well.

2. Numerical research

2.1. Governing equations

We consider a loop, placed in a vertical plane, which is heated at constant temperature T_h, over the bottom half and cooled at constant temperature T_c, over the top half. The boundary conditions are similar to those in [18], where the flow may take place due to buoyancy formed by a negative vertical temperature gradient.

For the numerical analysis of the thermosyphon, the flow was supposed to be three-dimensional, and all three velocity components and pipe curvature were included. The only simplifying assumptions were that:

1. The flow was symmetric about the vertical plane containing the circle of radius formed by the pipe centerline.
2. The flow was laminar and incompressible.
3. The flow had negligible Coriolis acceleration and negligible centripetal acceleration.
4. The flow and porous matrix had constant properties (except for the use of the Boussinesq approximation for the density of fluid, that $\rho_f = \rho_c[1 - \beta(T - T_c)]$), which are isotopic and homogeneous.
5. The solid matrix and liquid are in well energy equilibrium.

Those assumptions are usually believed to introduce little difference into the numerical solution from the real one [22,23].

The dimensionless form of the governing equations for steady flow expressed in the coordinate system in Fig. 2, are as follows, where u, v, w and Φ are all local volume-averaged values [23,24].

Continuity

$$\frac{\partial}{\partial r}(h_\varphi h_\theta u) + \frac{\partial}{\partial \varphi}(h_r h_\theta v) + \frac{\partial}{\partial \theta}(h_r h_\varphi w) = 0, \tag{1}$$

r-Momentum

$$u + C'_E|u|u = -\frac{\partial P}{\partial r} + Ra\Phi \sin\theta\cos\varphi + \frac{Da}{\varepsilon}\left(\nabla^2 u + S_{du}\right), \tag{2}$$

φ-Momentum

$$v + C'_E|v|v = -\frac{\partial P}{r\partial \varphi} - Ra\Phi \sin\theta\sin\varphi + \frac{Da}{\varepsilon}\left(\nabla^2 v + S_{dv}\right), \tag{3}$$

θ-Momentum

$$w + C'_E|w|w = -\frac{\partial P}{(R + r\cos\varphi)\partial\theta} + Ra\Phi\cos\theta + \frac{Da}{\varepsilon}\left(\nabla^2 w + S_{dw}\right), \tag{4}$$

Energy

$$(V\cdot\nabla)\Phi = \nabla^2\Phi, \tag{5}$$

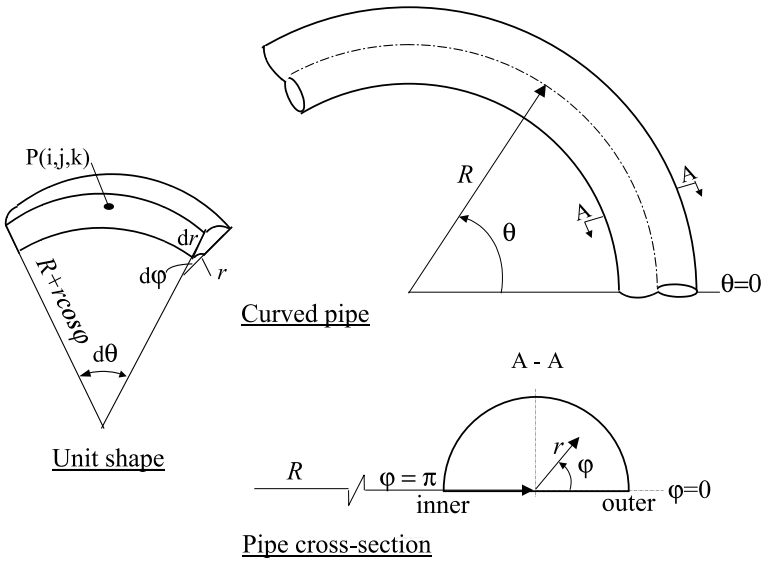

Fig. 2. The coordinate system for numerical programming.

where $h_r = 1$, $h_\varphi = r$, $h_\theta = R + r\cos\varphi$ are the Lamé coefficients in coordinate transformation;

$$(V\cdot\nabla) = \frac{1}{h_r h_\varphi h_\theta}\left[\frac{\partial}{\partial r}(uh_\varphi h_\theta\cdot) + \frac{\partial}{\partial\varphi}(vh_r h_\theta\cdot) + \frac{\partial}{\partial\theta}(wh_r h_\varphi\cdot)\right],$$

$$\nabla^2 = \frac{1}{h_r h_\varphi h_\theta}\left[\frac{\partial}{\partial r}\left(\frac{h_\varphi h_\theta}{h_r}\cdot\frac{\partial}{\partial r}\right) + \frac{\partial}{\partial\varphi}\left(\frac{h_r h_\theta}{h_\varphi}\cdot\frac{\partial}{\partial\varphi}\right) + \frac{\partial}{\partial\theta}\left(\frac{h_r h_\varphi}{h_\theta}\cdot\frac{\partial}{\partial\theta}\right)\right]$$

are differential operators; and

$$S_{d,u} = -\frac{2}{r^2}\frac{\partial v}{\partial\varphi} - \frac{u}{r^2} + \frac{\sin\varphi}{r(R+r\cos\varphi)}v + \frac{\cos\varphi}{(R+r\cos\varphi)^2}\left(v\sin\varphi - u\cos\varphi - 2\frac{\partial w}{\partial\theta}\right),$$

$$S_{d,v} = \frac{2}{r^2}\frac{\partial u}{\partial\varphi} - \frac{v}{r^2} - \frac{\sin\varphi}{r(R+r\cos\varphi)}u + \frac{\sin\varphi}{(R+r\cos\varphi)^2}\left(v\sin\varphi - u\cos\varphi - 2\frac{\partial w}{\partial\theta}\right),$$

$$S_{d,w} = \frac{2}{(R+r\cos\varphi)^2}\left(\frac{\partial u}{\partial\theta}\cos\varphi - \frac{\partial v}{\partial\theta}\sin\varphi - \frac{w}{2}\right)$$

are the transform products.

For Darcian flow, Eqs. (2)–(4) are much simplified as follows:

$$u = -\frac{\partial P}{\partial r} + Ra\Phi\sin\theta\cos\varphi, \tag{6}$$

$$v = -\frac{\partial P}{r\partial\varphi} - Ra\Phi\sin\theta\sin\varphi, \tag{7}$$

$$w = -\frac{\partial P}{(R+r\cos\varphi)\partial\theta} + Ra\Phi\cos\theta. \tag{8}$$

The porosity is considered as a const that $\varepsilon = 0.4$.

C'_E is derived by Ergun geometrical function

$$C_E = \frac{1.75}{(150\varepsilon^3)^{0.5}},$$

or

$$C'_E = \frac{1.75}{(150\varepsilon^3)^{0.5}}\cdot\frac{Da^{0.5}}{Pr}. \tag{9}$$

The dimensionless boundary conditions are:

1. zero velocity at wall: $u, v, w|_{r=1} = 0$,
2. specified wall temperatures in cooling section: $\Phi|_{r=1} = 0, \alpha \leqslant \theta \leqslant \pi + \alpha$ and in heating section: $\Phi|_{r=1} = 1, \pi + \alpha \leqslant \theta \leqslant 2\pi + \alpha$,
3. symmetry about the plane $\Phi = 0, \pi : \frac{\partial}{\partial\varphi}|_{\varphi=0,\pi} = 0$,
4. periodicity in θ direction: $u, v, w, \Phi, P|_{\theta=0} = u, v, w, \Phi, P|_{\theta=2\pi}$.

2.2. Numerical scheme

The differential equations were solved using a finite difference computer program in FORTRAN language in the coordinate system shown in Fig. 2. The staggered grids were used, where the control volumes of *u, v* and *w* were a half grid ahead of the main control volume of *P* and Φ in r, φ and θ directions, respectively. A central differencing method with second-order precision was used. The program consulted that of [25,26] in treating the singular units at the centerline. The SIMPLER algorithm determined the pressure.

Multi-grid strategy: Due to the contradiction between the special toroidal geometry and the limitation of the node number, the length in the θ direction of the grid $(R + r\cos\varphi)\Delta\theta$ is much larger than those in the radial direction Δr and in φ direction $r\Delta\varphi$ (see Fig. 2) if *R* is quite large. The iteration does not converge in this case because the coefficients of the difference equation are highly anisotropic. That difficulty was overcome by the multi-grid strategy. A block correction multi-grid method proposed by Hutchinson and Raithby ([27], the 1D2DAC manner, three grid layers) was introduced to improve the convergence of pressure equation (mass equation) and energy equation. This method had an additive advantage that the mass and energy conservations in the whole space were automatically satisfied when the iteration converged.

Computation flow: The procedure had converged values independent of grid when the grid was as fine as $40 \times 30 \times 100$ nodes (in the r, φ and θ directions, respectively). The *r* cells were not uniform, with finer spacing near the wall. The θ cells were finer near the connections of the heating and cooling halves. The wall was set for insulation at the connections $(\theta - \alpha = 0, \pi)$ to avoid singularity. The convection simulation started from an initial velocity field $w(r) = 1 - r^2$ and its consistent temperature field. In all calculations presented here, under relaxation factors of 0.35, 0.45,0.25,0.75 and 0.8 were applied to *u, v, w, P* and Φ (SLUR iterate). The equations were solved with an alternating direction implicit (ADI) method. The pressure correction is solved iteratively until the sum of absolute residuals has fallen by a factor of 10. The additive block correction was performed at each time of *P* and Φ calculation and was done once per 10 times of pressure correction. The calculation was finished when the residual sum over all the nodes of each equation is less than 1×10^{-4}, or

$$\frac{\sum\left|\Theta^m_{i,j,k} - \Theta^{m-1}_{i,j,k}\right|}{\sum\left|\Theta^m_{i,j,k}\right|} \leqslant 1\times10^{-4} \quad \Theta = u, v, w, P, \Phi. \tag{10}$$

The iteration is about 2000 times which costs half a day at a PC with Pentium 700 MHz CPU.

Code validity: The computer program was validated on several cases for which experimental data or

analytical solutions were available. These cases were chosen so as to verify that the distinct aspects of the computer program were properly implemented. The cases were:

1. two-dimensional natural convection in a porous annulus,
2. three-dimensional natural convection in porous media in a rectangular cavity,
3. three-dimensional natural convection in Newtonian fluid in the same torus as that in Lavine et al. [26].

Satisfactory agreement was obtained in every case.

2.3. Results and discussion

The flow behaviors depend on the five parameters *Ra*, *Pr*, *Da*, *R* and α. The multi-grid strategy significantly broadens the value scope of *Ra* so as to widely investigate the effects of those parameters. We firstly discuss a typical solution at $Ra = 50$, $Pr = 1$, $Da = 10^{-4}$, $R = 5$, $\alpha = 10°$, and then sum up the effects of some of those parameters on flow behaviors.

Flow patterns: Since $\alpha > 0$, the main flow is counterclockwise. However, regions of flow reversal do exist at both connections. Secondary or cross-stream motion (i.e., motion perpendicular to the θ direction) was also predicted by the numerical analysis.

Fig. 3 shows the temperature and the axial velocity fields in the symmetry plane and a cross-sectional plane. At the connections of the cooling half and the heating half, intensive local flow reversals exist. The detailed process is described by the following figures.

Fig. 4 shows the cross-sectional profiles of the temperature and axial velocity at the neighborhood of the right connection. In Fig. 4(a), before the flow enters the cooling half ($\theta - \alpha < 0$) the temperature curve is concave, of which the edges keep at the highest value ($\Phi = 1$) as the heating wall. The valley, formed by the inversed flow coming from the entrance of the cooling section, is at the inner wall. The inverse flow is heated by the wall, rises up due to buoyancy and is brought back by the main flow. Here an intensive secondary flow toward the outer wall is formed (see Fig. 5(a)). At the entrance to the cooling half ($\theta - \alpha > 0$), the temperature curve is convex, of which the edges keep at the lowest value ($\Phi = 0$) as the cooling wall. The peak formed by the hotter main flow is at the outer wall, which is quickly cooled. The cooled liquid decelerates, of which some amount starts to flow down along the inner wall to form the above-mentioned inverse flow. As a result, a secondary flow toward the inner wall is formed

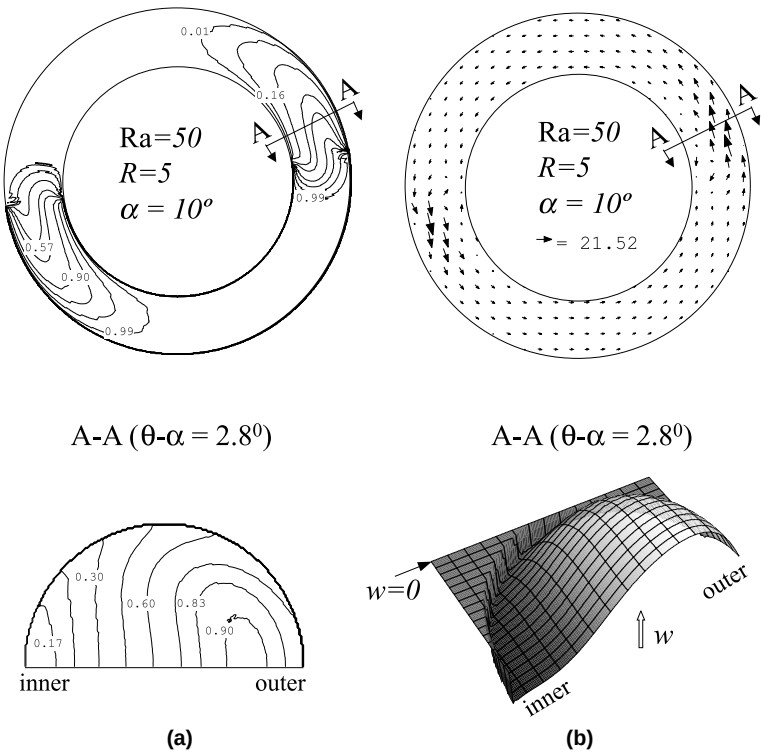

Fig. 3. An example of typical temperature contours (a) and flow fields (b) ($Ra = 50$, $Pr = 1$, $Da = 10^{-4}$, $R = 5$, $\alpha = 10°$).

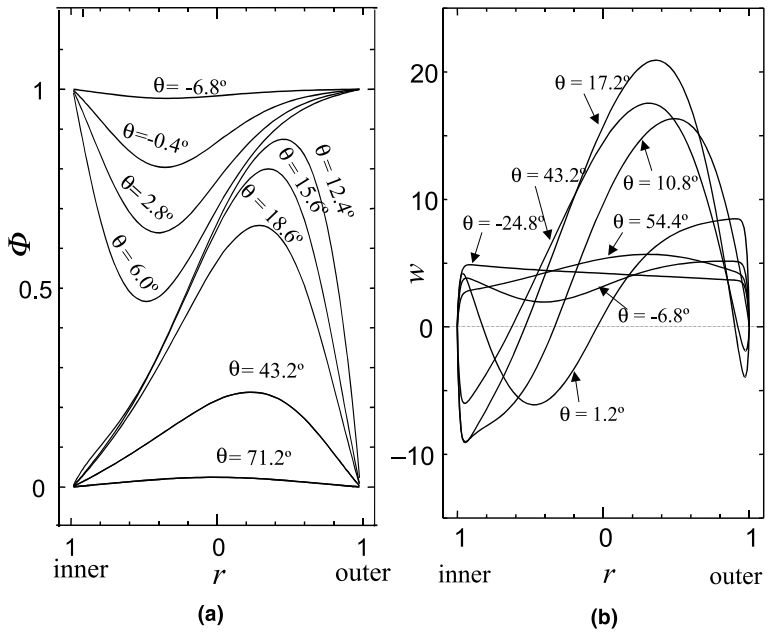

Fig. 4. Temperature and axial velocity profiles in different cross-sectional planes ($Ra = 50$, $Pr = 1$, $Da = 10^{-4}$, $R = 5$, $\alpha = 10°$).

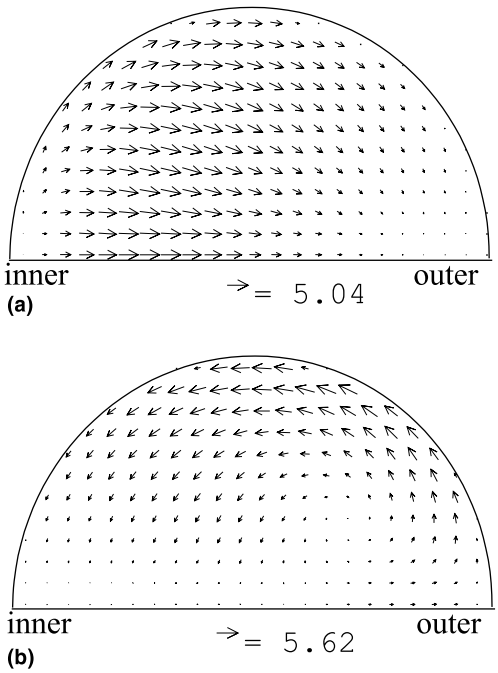

Fig. 5. The secondary flow near the right connection ($Ra = 50$, $Pr = 1$, $Da = 10^{-4}$, $R = 5$, $\alpha = 10°$). (a) $\theta - \alpha = -2.8°$; (b) $\theta - \alpha = 2.8°$.

(see Fig. 5(b)). Next, the axial velocity profiles in Fig. 4(b) demonstrate the variance of the inverse flow and main flow distributions along the torus. The shift is consistent with that of the temperature shown in Fig. 4(a). The local flow reversal at the left connection can also be reasoned in a similar way.

From those in Newtonian fluid, the temperature and axial velocity fields of the flow in porous media mainly differ in two ways. Firstly, the local flow re-circulation only exists at the neighborhood of the connections, although it wholly prevails in Newtonian fluid [25,26]. In fact the heat transfer between fluid and tube wall is already finished shortly after entering the entrances because the flow speed is very low ($Re \approx 8$). The porous matrix also quickly attenuates any axial vortex appeared in the main flow. Since it is caused by the transverse temperature gradients, the local inverse flow will not take place if the fluid uniformly keeps at the same temperatures as the walls. Secondly, in the area without flow reversal, the flow velocity only varies in the vicinity of the wall, which is the common feature of Darcian flow. The resulted flow profile is a flat hat (see $\theta = -24.8°$ in Fig. 4(b)) but not a parabola.

According to the definitions of the velocity weighted bulk temperature Φ_b and the area weighted average temperature $\bar{\Phi}$, their difference also reflects the irregularity of the axial velocity spatial distribution. The nature provides an alternative way to determine the extent of the flow field irregularity. Fig. 6(a) shows that the difference can only be distinguished at the neighborhood of the two connections. Near the entrance to the cooling half, the region of higher temperature is associated with higher velocity. Thus, the bulk temperature Φ_b will tend to be larger than the average temperature $\bar{\Phi}$. Similarly,

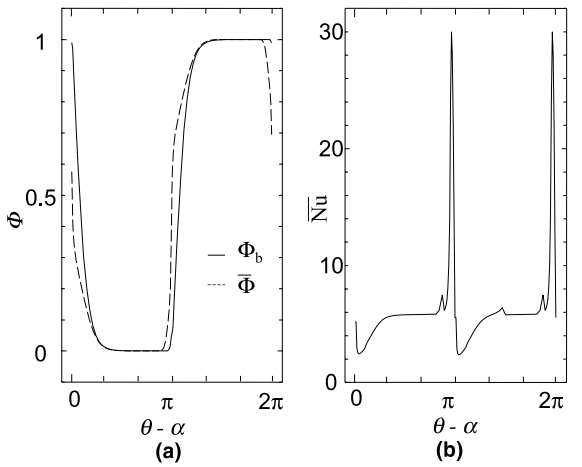

Fig. 6. Average and bulk temperatures (a) and Nusselt number (b) as functions of θ ($Ra = 50$, $Pr = 1$, $Da = 10^{-4}$, $R = 5$, $\alpha = 10°$).

near the heating section entrance, the region of higher temperature is associated with lower or even negative velocity. Thus the bulk temperature will tend to be lower in this region than the average temperature.

The peripherally averaged Nusselt number $\overline{\mathbf{Nu}}$ is shown in Fig. 6(b) as a function of θ. The Nusselt number decreases rapidly near the cooling and heating section entrances, as a thermal boundary layer develops. Throughout the remainder of the thermosyphon, however, $\overline{\mathbf{Nu}}$ varies non-monotonically with θ.

Fig. 7 shows the pressure field in the symmetry plane. The highest pressure is at the entrance to the cooling section. From here to the bottom, the potential gradually decreases along the torus at a variational speed. This is a pressure consuming section, in which the flow is driven by pressure potential. The pressure decreases quicker at the entrance quarter of the heating section because the flow has to overcome the inversed buoyancy. From bottom to the entrance to the cooling section, the pressure increases along the flow. This is a pressure accumulating section, in which the flow is driven by buoyancy. Because the flow in the pressure accumulating section is driven by buoyancy, the formed pressure gradients are different from that in the other section. Fig. 7 shows that in the vicinity of the bottom the pressure vertically varies, while in the other section it axially varies.

Flow behavior variation with Rayleigh number for $\alpha \neq 0$. Varying the Raleigh number Ra while keeping the other parameters at $Pr = 1$, $Da = 10^{-4}$, $R = 5$, $\alpha = 10°$ can reflect the effects of heating power. The average axial velocity $\bar{w}$ increases linearly with Ra as shown in Fig. 8. $\bar{w}$ is less than one ($Re < 2$) when $Ra < 20$, which means the convection is even slower than the heat diffusion. The convection is not distinguishable in practice. Fig. 9

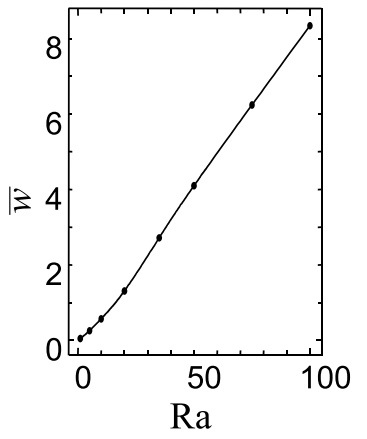

Fig. 8. Average axial velocity as a function of the Rayleigh number ($Pr = 1$, $Da = 10^{-4}$, $R = 5$, $\alpha = 10°$).

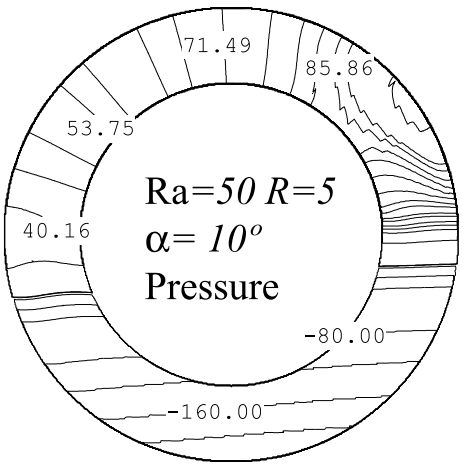

Fig. 7. A typical pressure contour in symmetric vertical plane ($Ra = 50$, $Pr = 1$, $Da = 10^{-4}$, $R = 5$, $\alpha = 10°$).

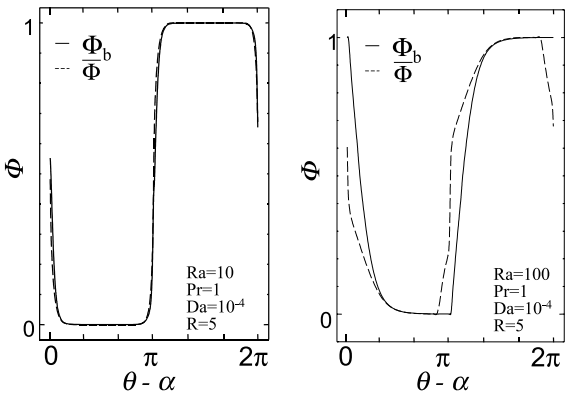

Fig. 9. Axial distributions of bulk and average temperatures at $Ra = 10$ and 100 ($\alpha = 10°$).

shows the axial profiles of the bulk temperature Φ_b and the average temperature $\bar{\Phi}$ as functions of θ at different Ra. For small Ra ($Ra = 10$), the discrepancy between Φ_b and $\bar{\Phi}$ is undistinguishable, which suggests that both the convection and flow reversal are faint. As Rayleigh number becomes larger ($Ra = 100$) this discrepancy near the connections also increases. This implies that the local flow reversals there become more and more intensive. Since the average velocity $\bar{w}$ still increases linearly with Ra as shown in Fig. 8, the effects of flow reversal on driving force are negligible.

Flow behavior variation with Rayleigh number for $\alpha = 0$. As the Rayleigh number increases, the transition of flow patterns under symmetric boundary conditions ($\alpha = 0$) differs from that under the asymmetric ones. Let $Pr = 1$, $Da = 10^{-4}$, $R = 2$, $\alpha = 0$ and keep in mind that the simulation starts from a positive counter-clockwise flow field. The converged flow field is different for different Ra. Two typical results are shown in Fig. 10. If Rayleigh number is less than a certain critical value Ra_c, no global flow appears in the torus (Fig. 10(a)). However, two roll-like local convections exist at the connections. The rolls only spread to a short distance, and the fluid in the rest sections remains at static states without any flow motion and heat transfer. If $Ra > Ra_c$, a solution with counter-clockwise global flow was gotten. Fig. 10(b) shows that the field structure is similar to the above-motioned one at $\alpha = 10°$. When the simulation started from a clockwise flow field similar results were gotten. The iteration converged at the same solution as Fig. 10(a) if $Ra < Ra_c$, otherwise a solution with clockwise global flow that is bilateral symmetric with Fig. 10(b) were obtained. This suggests that the global flow happens only if the Rayleigh number is larger than a critical value. The critical value Ra_c rapidly increases with the torus main Radius R. For example, Ra_c is between 15 and 20 when R is 2, while Ra_c is larger than 100 when R equals 5.

Non-Darcian effects on flow behavior: The non-Darcian terms act on the flow behaviors in a very compli-

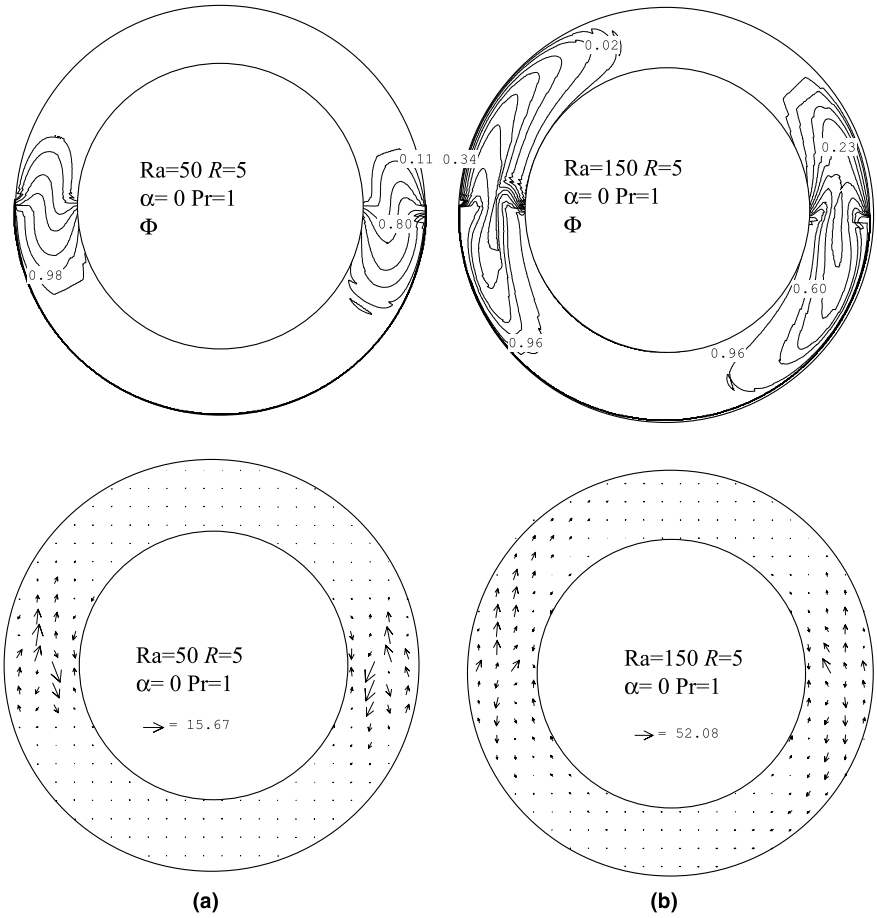

Fig. 10. Two typical temperature contours and flow fields at different Ra under symmetric boundary conditions. (a) $Ra = 50$; (b) $Ra = 150$.

cated way. The effect can be usually neglected for small Da and Ra. For example, the average axial velocity $\bar{w}$ is 1.310 for Darcian flow and 1.307 for non-Darcian flow at the parameters of $Ra = 50$ and $Da = 10^{-4}$.

3. One-dimensional formulation

Numerical results showed that the three-dimensional inversed flow only prevails near the connections. From both the views of friction and buoyancy, the one-dimensional formulation is reasonable at moderate Rayleigh number.

3.1. Modeling

We consider the flow motion in the thermosyphon filled with porous media under symmetric boundary conditions ($\alpha = 0$). The full form of the momentum equation with dimensions is

$$\frac{\rho_c}{\varepsilon}\frac{D\vec{V}}{Dt} = -\nabla P + \rho_f \vec{g} + \frac{\mu}{\varepsilon}\nabla^2\vec{V} - \frac{\mu}{K}\vec{V} - \frac{C_E}{K^{1/2}}\rho_c\left|\vec{V}\right|\vec{V}. \tag{11}$$

By making $u, v = 0$ and substituting the axial velocity for average value w^* (where $\partial w^*/\partial\theta = 0$), Eq. (11) is rewritten as follows:

$$\frac{\rho_c}{\varepsilon}\frac{dw^*}{dt} = -\frac{dP^*}{R^* d\theta} + g\beta(T - T_c)\cos\theta - \frac{\mu}{K}w^* - \frac{C_E}{K^{1/2}}\rho_c|w^*|w^*. \tag{12}$$

We integrate Eq. (12) to eliminate the pressure term and transform the resulted equation into dimensionless form, that is,

$$Pr'\frac{d\bar{w}}{d\tau} = \frac{Ra}{2\pi}\int_0^{2\pi}\Phi\cos\theta\, d\theta - \bar{w} - C'_E\left|\bar{w}\right|\bar{w}, \tag{13}$$

where $Pr' = (\sigma\varepsilon/Da)Pr$ is the equivalent Prandtl number of the porous medium.

Following that given in [21], consider an infinitesimal cylindrical control volume of fluid in the loop, with volume $\pi r^2 R^* d\theta$. The rate of change of thermal energy in the control volume is $\rho_f c\pi r_0^2 R^* d\theta(\sigma\frac{\partial T}{\partial t} + \frac{w^*}{R^*}\frac{\partial T}{\partial\theta})$, which must equal the amount of heat entering the control volume. The heat entering the control volume is $-2\pi r_0 R^* d\theta \cdot h(T - T_c)$ in the upper half or $2\pi r_0 R^* d\theta \cdot h(T_h - T)$ in the bottom half. The energy conversation equation can be written

$$\rho_f c\left(\sigma\frac{\partial T}{\partial t} + \frac{w^*}{R^*}\frac{\partial T}{\partial\theta}\right) = \begin{cases} -2h(T - T_c)/r_0, & 0 < \theta \leqslant \pi, \\ 2h(T_h - T)/r_0, & \pi < \theta \leqslant 2\pi. \end{cases} \tag{14}$$

Eq. (14) can be made dimensionless in the same way as in Section 2, or

$$\left(\frac{\partial\Phi}{\partial\tau} + \frac{\bar{w}}{R}\frac{\partial\Phi}{\partial\theta}\right) = \begin{cases} -Nu\Phi, & 0 < \theta \leqslant \pi, \\ Nu(1 - \Phi), & \pi < \theta \leqslant 2\pi. \end{cases} \tag{15}$$

Eqs. (13) and (15) are the one-dimensional governing equations of Darcian flow in the torus. In order to find the ordinary differential equations, we expand Φ in a Fourier series $\Phi = a_0(\tau) + \sum a_n(\tau)\cos n\theta + \sum b_n(\tau)\sin n\theta$ and substitute the series into two equations. Multiplying the resulted equation of Eq. (15) by each $\cos n\theta$ or $\sin n\theta$, respectively, and integrating the produced equations from 0 to 2π can decouple $a_0(\tau)$ $a_n(\tau)$ and $b_n(\tau)$. The equations for $\bar{w}$, $a_1(\tau)$ and $b_1(\tau)$ are independent of the others, which are:

$$dx/d\tau = Pr'(0.5Ra \cdot y - x - C'_E x|x|), \tag{16}$$

$$dy/d\tau = -Nu \cdot y - xz/R, \tag{17}$$

$$dz/d\tau = -4Nu/\pi - Nu \cdot z + xy/R, \tag{18}$$

where $x = \bar{w}$, $y = a_1(\tau)$, $z = b_1(\tau)$.

(Since $a_0(\tau)$ represents the average temperature of the whole torus and has no influence on the flow stability, we get the first right-hand term in Eq. (18) taking the steady value that $a_0(\tau) = 0.5$.)

3.2. Discussion

The model described by Eqs. (16)–(18) is also a Lorenz system, which is similar in form to that for Newtonian flow in [21] except with the different coefficients. This is natural because the pure fluid can be regarded as porous media in the limit of the porosity $\varepsilon = 1$. For example, Eq. (11) becomes N–S equation as ε increases to unit. However, the flow behaviors are diverse with variation in the equivalent Prandtl number Pr'.

We omit the Forchheimer term in Eq. (16) to simplify the analysis. The three steady state points are $(0, 0, -4/\pi)$ and

$$\left[\pm NuR\left(\frac{2Ra}{\pi NuR} - 1\right)^{0.5}, \pm\frac{2NuR}{Ra}\left(\frac{2Ra}{\pi NuR} - 1\right)^{0.5}, -\frac{2NuR}{Ra}\right],$$

which stand for the static heat conduction and steady flow in clockwise (−) and counter-clockwise (+) directions. The steady states are independent of the Prandtl number.

The two eigenvalues of the coefficient matrix at $(0, 0, -4/\pi)$ are:

$$\lambda_1 = -Nu, \quad \lambda_2 = 2Ra/\pi R - Nu. \tag{19}$$

According to the Center Manifold theory in non-linear dynamics [28], a saddle-node bifurcation takes place at $Ra \geqslant Ra_c = \pi NuR/2$, where the static heat conduction state gives way to the steady clockwise (−) or counter-clockwise (+) flow. The critical Rayleigh number Ra_c increases with the torus radius R which agrees with the numerical results. The longer the torus perimeter is, the

larger the flow friction is. The global flow cannot occur if the buoyancy due to temperature perturbation cannot overcome the friction. Before flow appears, the Nusselt number Nu should be strictly one and hence $Ra_c = \pi R/2$. However, the numerical results predicted two local convection areas near the connections before global flow appears. Hence the real critical Rayleigh number for steady global convection occurring should be larger than $\pi R/2$. The criterion for flow occurring is also unrelated to the Prandtl number.

Similar stability analysis is carried on the other two steady states. The characteristic equation of the coefficient matrix in either steady flow states is:

$$\lambda^3 + (Pr' + 2Nu)\lambda^2 + Nu\left(\frac{2Ra}{\pi R} + Pr'\right)\lambda + 2NuPr'\left(\frac{2Ra}{\pi R} - Nu\right) = 0, \tag{20}$$

which possesses one negative real and two conjugate complex solutions. The real parts of the two complex solutions become positive (the Hopf bifurcation) when the product of the coefficients of λ^2 and λ is less than the constant term, or

$$Ra > \frac{\pi R Pr'(Pr' - 4Nu)}{(3Pr' - 4Nu)}, \quad Pr' > 4/3Nu, \text{ or}$$

$$Ra < \frac{\pi R Pr'(Pr' - 4Nu)}{(3Pr' - 4Nu)}, \quad Pr' < 4/3Nu. \tag{21}$$

Negative Rayleigh number is meaningless. The Lorenz-like chaos could appear only if $Pr' > 4/3Nu$ and $Ra > ((\pi R Pr'(Pr' - 4Nu))/(3Pr' - 4Nu))$. The Rayleigh number criterion for chaotic flow increases with Pr'. As mentioned in the introduction, Pr' is a measure of the thermal inertia; a porous medium with small Pr' has either small friction or large thermal diffusivity, which

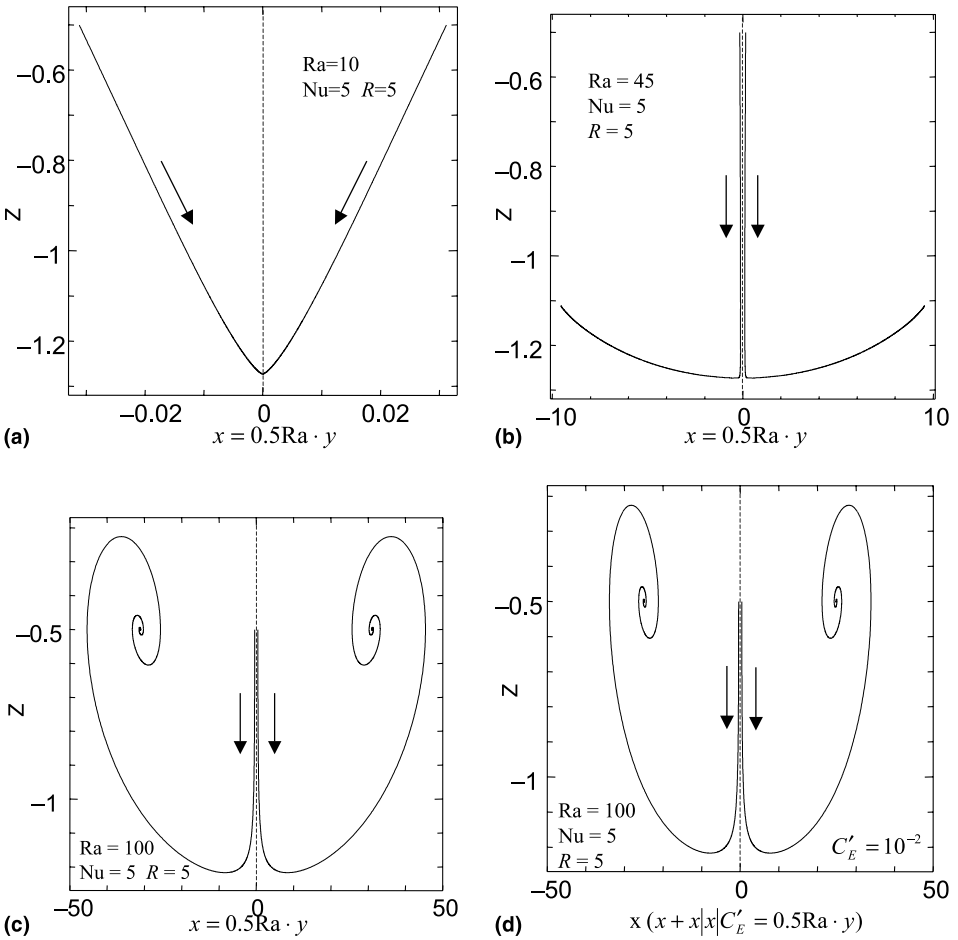

Fig. 11. Trajectories of Darcian flow at different Rayleigh numbers described by Eqs. (17), (18) and (22). (a) Stable static heat conduction; (b) stable steady convection, disturbance decaying without fluctuation; (c) stable steady convection, disturbance decaying with fluctuation (Darcian flow); (d) stable steady convection, disturbance decaying with fluctuation (Forchheimer flow).

favors the flow forming enough inertia force to reverse the flow direction. This is the case in [11,12].

On the contrary, in the limit of Darcian flow that $Pr' \to \infty$, the critical Rayleigh number goes to infinite as well. That means the global flow is always stable as is the case in Sen and Torrance [13]. For Darcy flow, Eq. (16) becomes,

$$x = 0.5Ra \cdot y \tag{22}$$

Eqs. (17), (18) and (22) describe another model resembling that in [13]. The model has the same solutions as those of Eqs. (16)–(18). The criterion for flow occurrence keeps also unchanged. But the two eigenvalues of the coefficient matrix in either steady flow state are:

$$\lambda_{1,2} = 0.5Nu\left\{ -1 \pm \left[1 + 4\left(\frac{2Ra}{\pi NuR} - 1\right)\right]^{0.5}\right\}. \tag{23}$$

Insofar as the global flow exists ($Ra_c > \pi NuR/2$), $\lambda_{1,2}$ are two negative real values if $Ra_c \leqslant 5\pi NuR/8$, and a couple of conjugate complex values with negative real part if $Ra_c > 5\pi NuR/8$. As a result, any disturbance to the flow will be decayed. At different Rayleigh number, the disturbance decaying modes are different. Fig. 11 shows the trajectories of flow converging at the steady states from fictional initial ones at different Rayleigh numbers, where the model was solved by a fourth-order Runge-Kutta method. If $Ra < \pi NuR/2$, the trajectories converge at static heat conduction state where $x = 0$ (Fig. 11(a)). In Fig. 11(b) where $\pi NuR/2 < Ra < 5\pi NuR/8$, the trajectories converge at the steady flows without fluctuation. When the two eigenvalues become complex, the trajectories still converge at the steady flows but in a periodic fluctuating mode (Fig. 11(c)). Fig. 11(d) shows the trajectories of Forchheimer flow, which is similar to Fig. 11(c) apart from its scope.

As shown by the numerical results the flow in the toroidal loop is almost one-dimensional due to the configuration. The instability of the thermal boundary layers can probably exist at high Rayleigh numbers but has insignificant effect on the global flow. Hence the conclusions drown above is reliable although it needs experimental verification.

4. Conclusions

Natural convection in a toroidal thermosyphon filled with porous media was numerically investigated and modeled. The numerical work aims to simulate the three-dimensional flow pattern and the variation of flow and heat transfer modes with the parameters. After the feasibility of one-dimensional formulating was examined, a one-dimensional model was proposed. Main conclusions were drawn as follows:

1. The numerical results showed that obvious local reversal flows exist near the two connections. The secondary flow shifts the cross-sectional distributions of the temperature and axial velocity. Comparing with the natural convection in Newtonian fluid, the local flow reversal in porous media only prevails a short distance from the connections and brings no apparent effects on the total friction and buoyancy. The average axial flow is also very slower than that in Newtonian fluid under the same heating power.
2. Under symmetric boundary conditions, the global flow appears only if the Rayleigh number is larger than a critical value. Although no global flow takes place at small Rayleigh number, two local natural convection rolls still exist near the connections.
3. The one-dimensional model showed that global flow occurs when Rayleigh number becomes larger than $\pi NuR/2$, which is smaller than the numerical values. The stability of global flow depends largely on the equivalent Prandtl number. The chaotic flow may appear at small Prandtl numbers but is absent in Darcian or Forchheimer flow. The results need experimental verification.

References

[1] J.M. Straus, Large amplitude convection in porous media, J. Fluid Mech. 64 (1974) 51–63.
[2] R.N. Horne, M.J. O'Sullivan, Oscillatory convection in a porous medium heated from below, J. Fluid Mech. 66 (1974) 339–352.
[3] J.P. Caltagirone, Thermoconvective instabilities in a horizontal porous layer, J. Fluid Mech. 72 (1975) 269–287.
[4] O. Kvernvold, On the stability of non-linear convection in a Hele–Shaw cell, Int. J. Heat Mass Transfer 22 (2) (1979) 395–400.
[5] H. Frick, U. Müller, Oscillatory Hele–Shaw convection, J. Fluid Mech. 126 (1983) 521–532.
[6] S. Kimura, G. Schubert, J.M. Straus, Route to chaos in porous-medium thermal convection, J. Fluid Mech. 166 (1986) 305–324.
[7] P.H. Steen, C.K. Aidun, Time-periodic convection in porous media: transition mechanism, J. Fluid Mech. 196 (1988) 263–269.
[8] M.D. Graham, U. Müller, P.H. Steen, Time-periodic thermal convection in Hele–Shaw slots; the diagonal oscillation, Phys. Fluids A 4 (1992) 2382–2393.
[9] M. de la Torre Juárez, F.H. Busse, Stability of two-dimensional convection in a fluid-saturated porous medium, J. Fluid Mech. 292 (1995) 305–323.
[10] W. Zimmermann, Effects of disorder in pattern formation, Phys. Rev. E 48 (4) (1993) 2699–2703.
[11] P. Vadasz, S. Olek, Transitions and chaos for free convection in a rotating porous layer, Int. J. Heat Mass Transfer 41 (11) (1998) 1417–1435.
[12] T. Masuoka, Some aspects of fluid flow and heat transfer in porous media, in: Proceedings of the 5th ASME/JSME

Joint Thermal Engineering Conference, AJTE99-6304, 1999.
[13] M. Sen, K.E. Torrance, Natural convection in a thin horizontal porous annulus, Int. J. Heat Mass Transfer 30 (4) (1987) 729–739.
[14] E.N. Lorenz, Deterministic nonperiodic flow, J. Atmos. Sci. 20 (1963) 130–141.
[15] J.H. Curry, J.R. Herring, J. Loncaric, S.A. Orszag, Order and disorder in two- and three-dimensional Bénard convection, J. Fluid Mech. 147 (1984) 1–38.
[16] H.F. Creveling, J.F. Depaz, J.Y. Baladi, R.J. Schoenhals, Stability characteristics of a single-phase convection loop, J. Fluid Mech. 67 (1975) 65–84.
[17] M. Gorman, P.J. Widmann, K.A. Robbins, Nonlinear dynamics of convection loop: A quantitative comparison of experiment with theory, Physica D 19 (1986) 255–267.
[18] P. Ehrhard, U. Muller, Dynamical behaviour of natural convection in a single-phase loop, J. Fluid Mech. 217 (1990) 487–518.
[19] Y. Wang, J. Singer, H.H. Bau, Controlling chaos in a thermal convection loop, J. Fluid Mech. 237 (1992) 479–498.
[20] P.K. Yuen, H.H. Bau, Optimal and adaptive control of chaotic convection-theory and experiments, Phys. Fluids 11 (6) (1999) 1435–1448.
[21] Y.Y. Jiang, M. Shoji, M. Naruse, Boundary condition effects on flow stability in a toroidal thermosyphon, Int. J. Heat Fluid Flow 23 (1) (2002) 81–91.
[22] A. Amiri, K. Vafai, Analysis of dispersion effects and non-thermal equilibrium, non-Darcian, variable porosity, incompressible flow through porous media, Int. J. Heat Mass Transfer 37 (5) (1994) 939–954.
[23] B. Alazmi, K. Vafai, Analysis of variants within the porous media transport models, ASME J. Heat Transfer 122 (1) (2000) 303–326.
[24] M. Kaviany, Principles of Heat Transfer in Porous Media, second ed., Springer, Berlin, 1995 (Chapters 1–4).
[25] A.-G. Lavine, A three-dimensional analysis of natural convection in a toroidal loop, PhD Dissertation, University of California, Berkeley, 1984.
[26] A.G. Lavine, R. Greif, J. Humphrey, 3-Dimensional analysis of natural-convection in a toroidal loop – effect of tilt angle, ASME J. Heat Transfer 108 (4) (1986) 796–805.
[27] B.R. Hutchinson, G.D. Raithby, A multigrid method based on the additive correction strategy, Num. Heat Transfer 9 (1986) 511–537.
[28] J.M.T. Thompson, H.B. Stewart, in: Nonlinear Dynamics and Chaos, seventh ed., Wiley, New York, 1993, pp. 108–128.